UCLA
UCLA Previously Published Works

Title

Electric field–catalyzed single-molecule Diels-Alder reaction dynamics

Permalink

https://escholarship.org/uc/item/2hs209sk

Journal

Science Advances, 7(4)

ISSN

2375-2548

Authors

Yang, Chen
Liu, Zitong
Li, Yanwei
et al.

Publication Date

2021-01-22

DOI

10.1126/sciadv.abf0689

Peer reviewed

Electric field–catalyzed single-molecule Diels-Alder reaction dynamics

Chen Yang[1]*, Zitong Liu[2]*, Yanwei Li[3,4]*, Shuyao Zhou[1], Chenxi Lu[3], Yilin Guo[1], Melissa Ramirez[3], Qingzhu Zhang[4], Yu Li[1], Zhirong Liu[1], K. N. Houk[3†], Deqing Zhang[2†], Xuefeng Guo[1†]

Precise time trajectories and detailed reaction pathways of the Diels-Alder reaction were directly observed using accurate single-molecule detection on an in situ label-free single-molecule electrical detection platform. This study demonstrates the well-accepted concerted mechanism and clarifies the role of charge transfer complexes with *endo* or *exo* configurations on the reaction path. An unprecedented stepwise pathway was verified at high temperatures in a high-voltage electric field. Experiments and theoretical results revealed an electric field–catalyzed mechanism that shows the presence of a zwitterionic intermediate with one bond formation and variation of concerted and stepwise reactions by the strength of the electric field, thus establishing a previously unidentified approach for mechanistic control by electric field catalysis.

INTRODUCTION

The Diels-Alder reaction is widely used in organic total synthesis of complex products (*1*, *2*) and was honored with the Nobel Prize in Chemistry in 1950 in anticipation of wide applications. The reaction generally proceeds by the concerted pericyclic mechanism involving a six-membered cyclic transition state to form both new bonds simultaneously. However, there is a continuous variation in mechanisms, from concerted or stepwise, not defined in terms of dynamics (*3*, *4*). The distinction between the two mechanisms in chemical reactions depends on the temporal resolution and detection sensitivity of the characterization method. Multiple processes that are faster than the time resolution of the monitoring instrument are often simplified as "concerted," while detection of intermediates during a reaction often provides evidence of a "stepwise" mechanism. For the Diels-Alder reaction, highly electronically complementary symmetrical diene and dienophile such as furan and maleimide (*5*, *6*) exhibit extremely small time differences (<5 fs) between the formations of the two bonds, which indicates a dynamically concerted mechanism. According to previous theoretical studies (*7*–*9*), only ~2% of the butadiene and ethylene reaction trajectories have wide potential energy surfaces and pass through diradical intermediates at 1000 K, implying a stepwise pathway. Another interesting theoretical work predicted that an external electrical field (EEF) could catalyze the Diels-Alder reaction and induce a mechanistic crossover from a concerted to a zwitterionic pathway (*10*). The experimental detection of trace and short lifetime reaction trajectories and proof of a stepwise pathway for a Diels-Alder reaction under such harsh conditions is a formidable challenge.

Single-molecule detection may be able to overcome these difficulties. The high temporal resolution detection of the dynamic behavior at the single-molecule/single-event level provides an opportunity to capture trace and short lifetime intermediates. Various conditions for single-molecule reactions have been studied including various temperatures (*11*), optical fields (*12*), magnetic fields (*13*), mechanical stimulation (*14*), and, more recently, the effects of electric fields (*15*–*18*), with these experiments aiming to manipulate single molecules and regulate the chemical reactions (*19*, *20*). The present work used an electrical monitoring platform based on graphene-molecule-graphene single-molecule junctions (GMG-SMJs) (*21*, *22*) to show that (i) a single-molecule connection can be directly characterized by photoelectric integration, (ii) stable covalent anchoring and determined interface coupling are suitable for complex reaction conditions, (iii) the fixed single-molecule system can provide in situ monitoring of reactions, and (iv) label-free high-speed electrical sampling of the molecular conductance provides high temporal resolution and faithful synchronization to the chemical reaction. Previous studies detecting intermolecular interactions (*23*, *24*) and chemical reactions (*25*, *26*) are extended here to offer the most complete description of single-molecule Diels-Alder reaction dynamic.

RESULTS AND DISCUSSION

Device fabrication and photoelectrical characterization

Prepared graphene transistors were etched by oxygen plasma using a poly(methyl methacrylate) (PMMA) template exposed by electron beam lithography to obtain carboxyl terminal graphene point electrode pairs. Molecular engineering was used to synthesize a molecular bridge with the maleimide functional center and amino terminals that were covalently integrated into graphene electrodes to form stable GMG-SMJs (Fig. 1A). Detailed molecular synthetic routes and the device preparation steps are given in the Supplementary Materials (figs. S1 to S3). The successful preparation of the GMG-SMJs was determined by comparing the current-voltage (*I-V*) relation curve after etching (decreased to zero) with the curve after connecting the molecules between source and drain electrodes (recovered to some extent) (fig. S4). With optimized conditions, the connection yield reached ~22% with about 20 of the 92 devices on the same silicon chip showing recovery of the current (fig. S5), which demonstrates the reproducibility. The statistical analysis in the Supplementary

[1]Beijing National Laboratory for Molecular Sciences, State Key Laboratory for Structural Chemistry of Unstable and Stable Species, College of Chemistry and Molecular Engineering, Peking University, Beijing 100871, P. R. China. [2]Beijing National Laboratory for Molecular Sciences, CAS Key Laboratory of Organic Solids, Institute of Chemistry, Chinese Academy of Sciences, Beijing 100190, P. R. China. [3]Department of Chemistry and Biochemistry, University of California, Los Angeles, Los Angeles, CA 90095, USA. [4]Environment Research Institute, Shandong University, Qingdao 266237, P. R. China.
*These authors contributed equally to this work.
†Corresponding author. Email: guoxf@pku.edu.cn (X.G.); dqzhang@iccas.ac.cn (D.Z.); houk@chem.ucla.edu (K.N.H.)
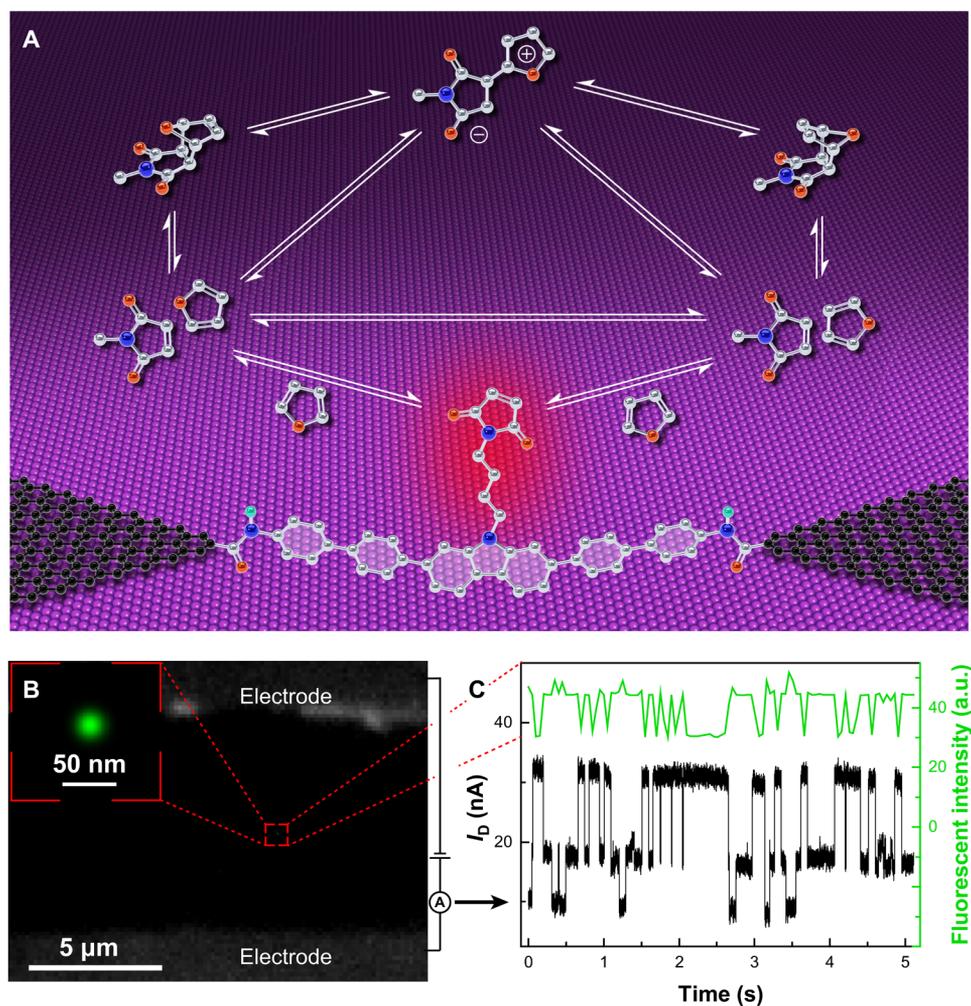
Fig. 1. Characterization of single-molecule devices. (A) Schematic diagram of the single-molecule electrical monitoring platform. **(B)** Demonstration of a single-molecule connection. During the interaction between single-molecule maleimide and fluorescein-substituted furan, 5000 photos taken by a superresolution fluorescence microscopy with 50-ms exposure are reconstructed to obtain a single-molecule resolution photograph and an enlarged image without the background. **(C)** Synchronous monitoring of current and fluorescent signals during the 5-s reaction. 10^{-5} M fluorescein-substituted furan in an ethanol/toluene (v/v: 2/3) solution was added to the reaction cell at 298 K and 300 mV. a.u., arbitrary units.

Materials demonstrates that the current response has ~90% probability of originating from only one molecular connection between the electrodes. The single-molecule connection can be further proven directly by superresolution microscopic imaging of the devices during the reaction between the fluorescein-substituted furan and maleimide functional center. The energy/electron transfer from fluorescein to the electrodes after adduction (27, 28) and the reversible reaction led to the fluorescein blinking and stochastic optical reconstruction microscopy effect (29). Only one bright spot was imaged between the graphene electrode arrays, which demonstrates the one-molecule connection (Fig. 1B; additional images and an image from a control device are provided in figs. S6 and S7). Furthermore, synchronous sampling of the fluorescent intensities and the electrical signals (the scheme is shown in fig. S8) reveals strong correlation (the highest conductance corresponds to the quenched florescence; the lowest conductance corresponds to the highest intensity florescence; and the middle conductances correspond to the relatively weak quenching; the attribution of the conductance states will be

provided below) that displays the dynamic behavior of the Diels-Alder reaction, which further confirms the optical and electrical monitoring results (Fig. 1C; details are provided in movie S1). This observation again strongly supports the single-molecule conjunction and shows that the molecular bridge is indeed the reaction center.

**Real-time electrical measurement and species attribution**

According to the theory of molecular electronics (30), the reaction center conductance is closely related to its structure during the reaction with furan. Therefore, a constant source-drain bias voltage was applied while recording the change in the conductance (current) using high-speed sampling [57,600 samples (Sa)/s] to monitor the structural changes during the chemical reaction in real time, which is the most intuitive analysis of the reaction mechanism and gives accurate measurements of the chemical reaction process. The single-molecule device was placed in a closed probe chamber with precise temperature control, while the maleimide on the molecular bridge reacted with furan in a gas phase under the protection of nitrogen. The

nanoampere-level current was measured while applying various constant bias voltages at 393 K with the measurements showing stochastic switching between six stable states corresponding to six different structures (Fig. 2A). Systematic control experiments demonstrated that there were no obvious fluctuations in the currents through the devices before connection (open circuit) (fig. S9), through graphene homojunction devices in a furan atmosphere (figs. S10 and S11), through the molecular bridge without the functional center (figs. S12 and S13), and through single-molecule devices without furan (figs. S14 and S15) in the same conditions. Thus, these results show that the monitored electrical signals originated from the reaction of the single-molecule maleimide with furan.

The corresponding species of the six conductive states [the statistical histograms are shown in Fig. 2 (A and B)] were determined on the basis of liquid-phase concentration and temperature-dependent measurements (figs. S16 to S20). At low concentrations, the lowest conductance state dominated the device conductance, demonstrating its attribution to the substrate. At low temperatures, the ratio of the second and third conductance states versus the substrate in-

creased with higher furan concentrations, confirming the formation of two conformed charge transfer complexes with *endo* or *exo* configurations. As the temperature increased, the fourth and fifth conductance states via corresponding complexes were observed, which should be ascribed to two target products. Stochastic spikes (the sixth conductance state) were observed in the pathway from the complexes to the products with high temperature and bias voltages (Fig. 2, A and B), implying the presence of a new (zwitterionic) intermediate. These speculations were further verified by the transmission calculation (Fig. 2C and fig. S21). As shown in fig. S21, the perturbed highest occupied molecular orbitals (p-HOMOs; the orbital scattering states of each species are provided in fig. S22) of each species dominate the charge transport (and, thus, the device conductance) because they are closer to the electrode Fermi level (0 eV). Correspondingly, the proximity of the transmission peaks to the electrode Fermi level (Fig. 2C) indicates that the molecular conductance sequence from low to high (the transmission peaks from left to right) should be the maleimide reactant state (RS), the charge transfer complex states (CTs) (because of the electron-deficient nature of the side-chain maleimide, it forms a CT complex with furan) (6), the product states (PSs), and the zwitterionic intermediate (ZI) (Fig. 2B), which has excellent agreement with the experimental observations in Fig. 2A. The conversion of the five lower conductance states with the fixed timing sequence relationship shown on the right of Fig. 2A displays the typical Diels-Alder reaction mechanism: The RS (red line) and furan first form *endo* (orange line) or *exo* (green line) CTs (CT-*endo* and CT-*exo*) and then produce corresponding PSs (light and dark blue lines) (PS-*endo* and PS-*exo*) through six-membered cycloaddition. The switching of the two pathways through the transformation of the CT configurations was also detected in the experiments, which shows the intrinsic concerted mechanism via either a kinetic or thermodynamic pathway (as discussed below). The *endo* pathway is more probable than the *exo* pathway, as indicated by the statistical histograms (Figs. 2B and 3), which shows the effect of secondary orbital and electrostatic interactions.

The highest conductance state (violet line) was attributed to a ZI instead of a diradical species because of its strong dependence on the bias voltage (appeared at 300 mV with a positive correlation with the bias voltage; Fig. 2A, left). This finding implies the opening of an unusual stepwise pathway at temperatures lower than 1000 K (7). Computational results show that $\Delta G^{\ddagger}$ for the stepwise mechanism was ~16 to 17 kcal/mol higher than for the concerted *endo*/*exo* mechanism for the conventional reaction in solution, which indicates a large preference for the concerted process (fig. S23). The strong polarity of the transition structure (TS; ~13.0 Debye) and ZI (~18.1 Debye) due to the large charge separation (fig. S24) implies that they will be notably stabilized by applying an EEF between the nanogapped graphene point electrodes (~10^9 V/m). The detailed structures and charge distributions of each species are provided in fig. S24. To verify this premise quantitatively, the influence of the EEF on the reaction of maleimide with furan was studied computationally (Fig. 2D). The models considered two orientations of the electric field with respect to the reactants, with stepwise-A (gray line) having the EEF orientated along the axis corresponding to the forming bond and stepwise-B (violet line) having the EEF orientated along the dipole moment vector that links the partial negative and partial positive charges (fig. S24). $\Delta G^{\ddagger}$ for stepwise-B is much lower than that of stepwise-A, which indicates that the EEF orientation along the line connecting the partial charges provides more stabilization
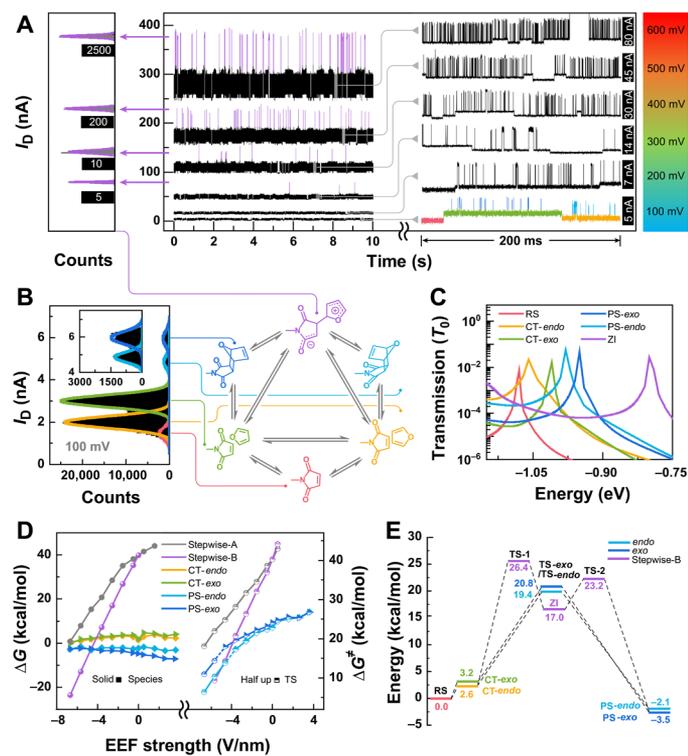
Fig. 2. Effect of an electric field on the Diels-Alder reaction. (**A**) Bias voltage–dependent experiments under 100 to 600 mV at 393 K. The right side is the zoom-in picture of the concerted reaction process. The left side is the statistical histogram of the highest conductivity state [zwitterionic intermediate (ZI)] under 300 to 600 mV. (**B**) Statistical histograms and reaction mechanism under 100 mV and the corresponding attribution of the six conductance states obtained from Gaussian fittings of *I-t* measurements. (**C**) Transmission spectra of six species, where the dominated transmission orbitals (p-HOMOs) are displayed. (**D**) Quantitative analysis of the EEF effect, showing that the calculated Gibbs free energies of each species (left) and transition states (right) change with the given electric field strength. This indicates that the strong EEF can overcome the huge disadvantage of the stepwise mechanism. (**E**) Gibbs free energies for the concerted and stepwise pathways at −2.57 V/nm.
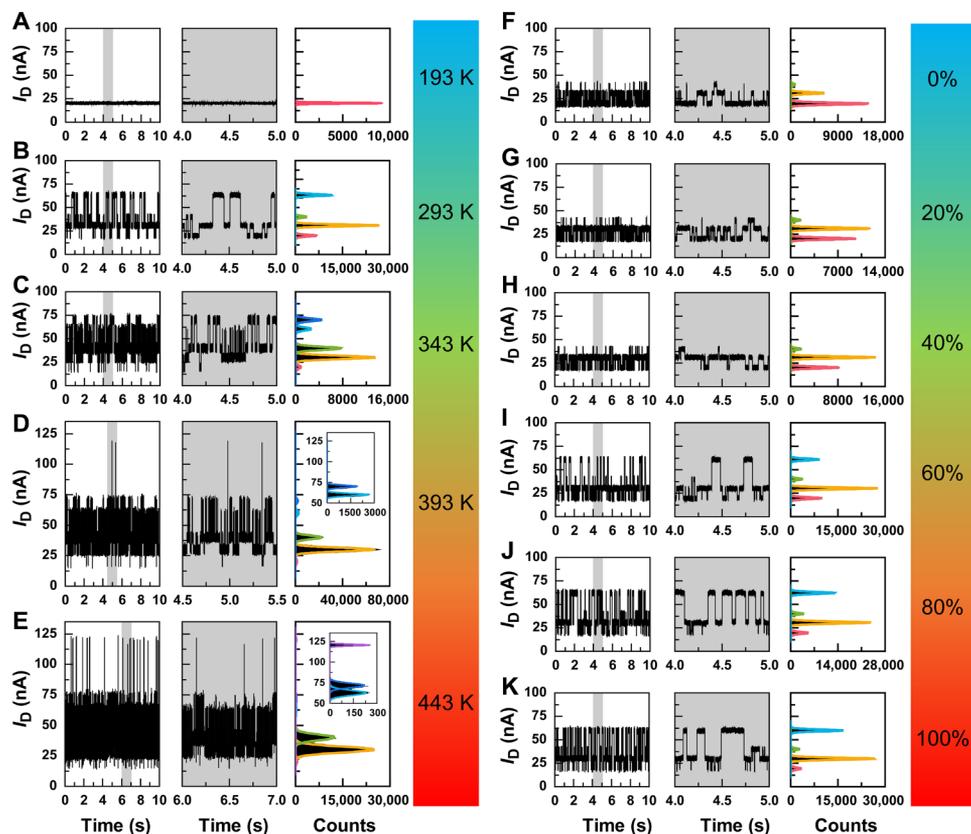
Fig. 3. Effects of temperature and polarity on the Diels-Alder reaction. (**A** to **E**) Typical *I-t* curves and corresponding enlarged images and statistical histograms at 193 K (A), 293 K (B), 343 K (C), 393 K (D), and 443 K (E). (**F** to **K**) *I-t* curves and corresponding enlarged images and statistical histograms measured in the solutions with 0% (F), 20% (G), 40% (H), 60% (I), 80% (J), and 100% (K) toluene in dimethyl sulfoxide (DMSO) at 298 K and 300 mV.

of the transition structure than the orientation along the reaction axis. In addition, the flexible carbon chain between the maleimide and the molecular bridge easily orientates ZI to the EEF, which also provides a preference for the stepwise-B orientation. It should be emphasized that strong EEF significantly lowers the energy barriers for both concerted and stepwise reactions. However, increasing the EEF strength can overcome the huge disadvantage of the stepwise mechanism. For example, at an EEF of −2.57 V/nm, $\Delta G^{\ddagger}$ for stepwise-B (~26.4 kcal/mol) is only 5.6 kcal/mol higher than the concerted *exo* pathway (~20.8 kcal/mol) (Fig. 2E) when accounting for the dependence of ZI on the bias voltage (Fig. 2A). Although $\Delta G^{\ddagger}$ for the stepwise mechanism is relatively high (e.g., −2.57 V/nm), increasing the temperature could enhance the reaction rate according to the Eyring equation [$k = (\kappa k_{B}T/h) \times \exp(-\Delta G^{\ddagger}/RT)$].

Temperature-dependent measurement

To verify this assumption, five representative temperature-dependent *I-t* curves at 300 mV are shown in Fig. 3 (A to E) and figs. S25 and S26. The furan could not be volatilized to the single-molecule reaction site because of the low saturation vapor pressure (~76 Pa, obtained from the Antoine equation) at 193 K. The measurement platform recorded only the conductance state of the maleimide substrate (Fig. 3A). The furan molecules (saturation vapor pressure, ~95 kPa) diffused to the single-molecule maleimide and converted to the *endo* product via the *endo* charge transfer complex

salts at room temperature (293 K), which indicates opening of the kinetic path (Fig. 3B). The kinetic and thermodynamic reaction paths both existed at the same time at 343 K and displayed five different current states (Fig. 3C), which is consistent with the liquid-phase temperature-dependent measurements (figs. S16 to S20). When the temperature was increased to 393 K, ZIs were occasionally observed, which represents the opening of the stepwise pathway (Fig. 3D). Higher temperatures created more reaction trajectories crossing the reaction energy barrier in the stepwise pathway and more ZI detected at 443 K (Fig. 3E). The temperature-dependent experiments well exemplified the three potential energy surfaces of the *endo/exo* concerted pathways and the stepwise pathway and demonstrated the strong regulation of the three pathways (Fig. 2B).

Solvent-dependent measurement

The reaction pathways can be regulated not only by temperature but also by an electric field, as summarized in figs. S27 to S29. The electric field can be adjusted by using solvents with different polarities to change the shielding effect to the electric field (*31*, *32*). The solvent-dependent measurements for various toluene to dimethyl sulfoxide (DMSO) ratios at 298 K were shown in Fig. 3 (F to K). (The influence from solvents was excluded through control experiments in fig. S30 and the results at other temperatures are shown in figs. S31 to S33.) The *I-t* curves show only the conversion between maleimide and CTs in DMSO, implying longer cycloaddition time
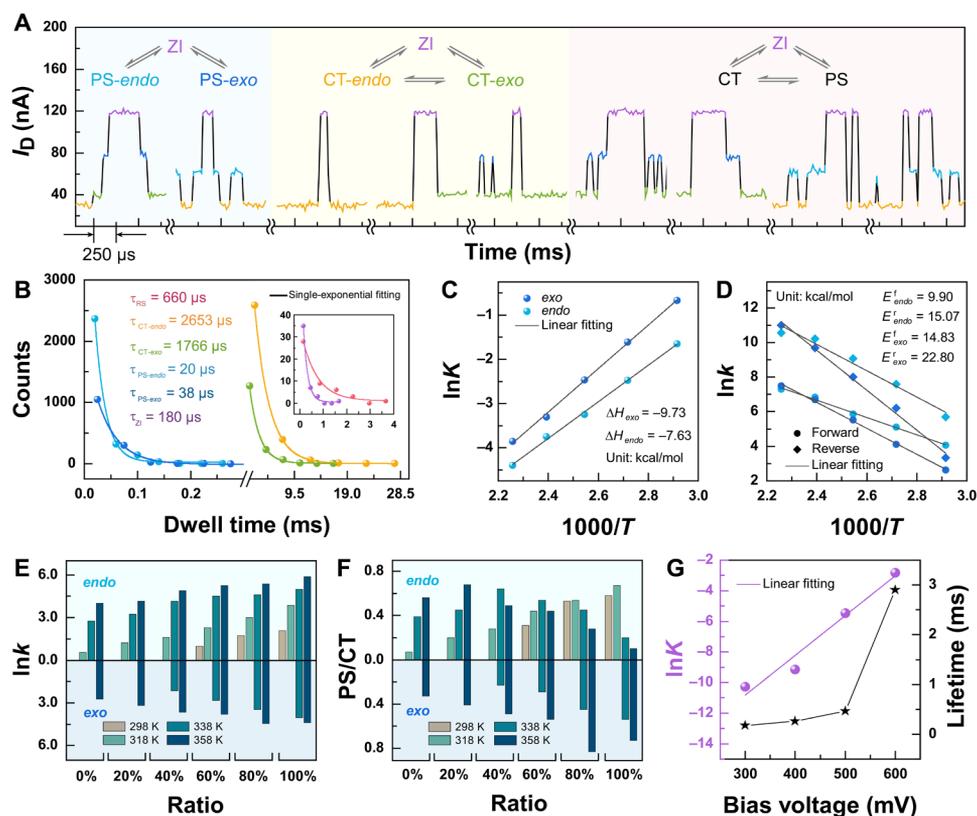
Fig. 4. Thermodynamic and kinetic properties of the single-molecule Diels-Alder reaction. (**A**) Time sequence of the transitions among different species during the Diels-Alder reaction. (**B**) Plots of time intervals of each conductance state and the lifetimes of each state obtained from single-exponential fittings. (**C**) Plots of the thermodynamic parameters ($\ln K$ versus $1000/T$) deduced from temperature-dependent measurements. ΔH of the two concerted pathways was derived from Van't Hoff equation. (**D**) Plots of kinetic parameters ($\ln k$ versus $1000/T$). The activation energies of the forward and reverse reactions of the two concerted pathways were obtained by Arrhenius equation. (**E**) Dependence of the reaction rate ($\ln k$) of the concerted pathway on the gradient ratio of toluene at 298, 318, 338, and 358 K. (**F**) Dependence of the product yield (PS/CT) of the concerted pathway on the gradient ratio of toluene at 298, 318, 338, and 358 K. (**G**) The approximately linear relationship of the equilibrium of ZI to other species ($\ln K$) with the applied bias voltage and the exponential correlation between its lifetime and bias voltage at 393 K.

scales than the monitoring window (10 s) and high energy barriers (Fig. 3F). As the proportion of toluene in the DMSO was increased, more cycloaddition behavior was observed, which indicates a decrease of the energy barrier (Fig. 3, G to K). This unique phenomenon can be attributed to quenching of the electrostatic catalysis in polar media. Quenching the electrostatic catalysis will significantly lower the barriers of the concerted pathway (Fig. 2D). Computational results also suggested that concerted *endo* mechanism changes to the stepwise mechanism at EEF $\leqq$ −4.63 V/nm while the concerted *exo* mechanism changes to the stepwise mechanism at EEF $\leqq$ −5.65 V/nm (Fig. 2D), which are difficult to achieve experimentally because of these high voltages. This mechanistic crossover has also been reported for the reaction of maleic anhydride with cyclopentadiene (*10*). In general, these density functional theory results show that the stepwise mechanism becomes competitive at −4.63 V/nm $\leqq$ EEF $\leqq$ −2.57 V/nm and dominates the reaction for EEF $\leqq$ −4.63 V/nm.

Kinetic and thermodynamic analysis

This article provides a detailed dynamic analysis of electrically catalyzed Diels-Alder reactions. The conversion network shown in Fig. 2B can be embodied in *I-t* curves. The two kinds of CT intermediates undergo concerted or stepwise mechanisms to generate *endo* or *exo* products. The stepwise pathway can also generate *endo* or *exo* products via the ZI reversibly (Fig. 4A). For the electrically catalyzed concerted mechanism, the equilibrium K at five temperatures in the range of 343 to 443 K (Fig. 4, B to E, and fig. S34) between the CTs and corresponding products can be derived from the ratio of the Gaussian fit peak areas in the *I-t* measurement statistical histograms. The lifetime (τ) of each species can be obtained through single-exponential fitting (Fig. 4B) of the time intervals in idealized *I-t* curves (fig. S35). The conversion rate constant, $k = 1/\tau$, can be obtained from a maximum interval likelihood rate estimate (*33*). Various thermodynamic (ΔG, ΔH, and ΔS) and kinetic parameters (E_a and $\Delta G^{\ddagger}$) were obtained using the Van't Hoff equation [$-RT\ln(K) = \Delta H - T\Delta S$] (Fig. 4C), Arrhenius plots (Fig. 4D), and the Eyring equation (detailed results are provided in table S1). K and $|\Delta G|$ were found to be lower than the theoretical results for 0 V/nm and observed results in the literature (*34*) and ^{1}H nuclear magnetic resonance (^{1}H NMR) macroscopic experiments (figs. S36 to S38), which implies distinct regulation of the equilibrium by the electric field. This phenomenon agrees with the variations of computationally determined G of CTs and PSs with the electric field strength shown in Fig. 2D. Similarly, the lower $\Delta G^{\ddagger}$ shows that electrical catalysis results are

consistent with simulation results (Fig. 2D). The experiments also show how the dynamic (Fig. 4E) and thermodynamic (Fig. 4F) processes are regulated by solvents (electric field) and temperature. Increased temperature and decreased polarity have positive effects on the cycloaddition rate (Fig. 4E) but have negative effects on the equilibrium. The product yield (PS/CT; Fig. 4F) reflects the antagonistic effect of the increased rate and decreased equilibrium. For the electrically catalyzed stepwise mechanism at 393 K, a theoretical calculation showed that the G of ZI decreases linearly with increasing electric field. The change in ΔG (from ZI to other species) with the bias voltage can be defined as $-RT\ln K = \Delta G \approx L \times V + \Delta G_0$, where L is the slope, V is the electric field strength, and ΔG_0 is ΔG at 0 V/nm. The equilibrium constant K for reactions from other species to ZI can be obtained from the ratio of the Gaussian fit peak areas of the corresponding conductance states. The linear relationship between $\ln K$ and the bias voltage in Fig. 4G shows the positive correlation between the electric field strength and the bias voltage. The definition of "V" can then be replaced by the bias voltage. Then, L was calculated as ~-0.02 kcal/(mol·mV), which semiquantitatively reflects the influence of the electric field on the species potential energy to lay a foundation for designing electric field–catalyzed organic synthesis reactions. In addition, the ZI lifetime can be regulated by the electric field due to exponential correlation (Fig. 4G), which provides future opportunities to capture short lifetime intermediates and to even detect the transition state (35), the holy grail of chemical reactions.

This work exemplifies a unique, unprecedented single-molecule electrical detection method to comprehensively analyze the Diels-Alder reaction process and elucidate the concerted pathway through the charge transfer complexes and the stepwise pathway via a new ZI, which provides infinite opportunities for understanding many indecipherable mechanisms in organic chemistry. The outstanding performance of the electrically catalyzed Diels-Alder reaction shows artificial modulation of both concerted and stepwise pathways as well as the reaction thermodynamics and kinetics, which lays a foundation for regulating chemical reaction and life science processes.

MATERIALS AND METHODS
Molecular synthesis
The details of molecular synthesis are provided in the Supplementary Materials.

Device fabrication and molecular connection
The method for preparation of graphene field-effect transistor (FET) and graphene point electrodes was described in figs. S2 and S3. A single-layer high-quality graphene was grown on a 25-µm-thick copper film (oxide removed) using a high-temperature, low-pressure chemical vapor deposition. PMMA 950 was spin-coated onto the graphene as the graphene-supporting layer and the copper films were etched by the FeCl$_3$ solution. Then, the graphene was transferred to a 1.5 cm by 1.5 cm precleaned silicon wafer with a 300-nm SiO$_2$ layer, and the PMMA was removed by acetone. After depositing a gold mark, the silicon chip was protected by a mask and etched by oxygen plasma to obtain a 40-µm-wide graphene strip. Eight-nanometer Cr and 60-nm Au were then thermal evaporated as metal electrode arrays using the template method. A 40-nm-thick SiO$_2$ layer was evaporated onto the metal electrodes to prevent current leakage in the solution phase. The prepared graphene FET was

etched using dashed line lithography through electron beam lithography, and a graphene electrode array with a carboxyl acid terminal was obtained by oxygen plasma etching and electrical burning. Freshly prepared graphene point electrode array devices were immersed in a pyridine solution containing 0.1 mM of the molecular bridge (deprotection of Boc by CF$_3$COOH) and 1 mM 1-(3-dimethylaminopropyl)-3-ethylcarbodiimide hydrochloride. After 48 hours, the devices were removed from the solution, rinsed with deionized water, and dried with flowing N$_2$. This connected a molecular bridge between the graphene electrode pairs with amide bonds.

Electrical characterization
The I-V curves were measured by an Agilent 4155C semiconductor parameter system and a Karl Suss (PM5) manual probe station. The I-t curves were obtained in vacuum cryogenic probe station (Lakeshore TTPX). The auxiliary output of the UHFLI lock-in amplifier gave a constant bias (100 to 600 mV) for the I-t curves. The current signal of the molecular loop was amplified by a DHPCA-100 amplifier and then recorded by high-speed acquisition card from NIDAQ at a sampling rate of 57,600 Sa/s.

Photoelectrical characterization
The self-built instrument was described in fig. S8. The molecular conductance and fluorescence were monitored simultaneously. The electron multiplying charge-coupled device (EMCCD) acquired photos with 50-ms exposures while the auxiliary output of the UHFLI lock-in amplifier gave a constant bias of 300 mV with the trigger from the control cable. Fluorescein-substituted furan was used to react with the single-molecule maleimide at the molecular bridge. The fluorescence was excited by a 405-nm laser and acquired by the EMCCD through a 100× objective lens. The electrical signal was amplified by a DL1211 preamplifier and recorded on a high-speed data acquisition card from NIDAQ at a sampling rate of 57,600 Sa/s in UHFLI.

SUPPLEMENTARY MATERIALS
Supplementary material for this article is available at http://advances.sciencemag.org/cgi/content/full/7/4/eabf0689/DC1

REFERENCES AND NOTES
1. A. Moyano, R. Rios, Asymmetric organocatalytic cyclization and cycloaddition reactions. *Chem. Rev.* **111**, 4703–4832 (2011).
2. R. B. Woodward, F. Sondheimer, D. Taub, K. Heusler, W. M. Mclamore, The total synthesis of steroids. *J. Am. Chem. Soc.* **74**, 4223–4251 (1952).
3. E. W.-G. Diau, S. De Feyter, A. H. Zewail, Femtosecond dynamics of retro Diels–Alder reactions: The concept of concertedness. *Chem. Phys. Lett.* **304**, 134–144 (1999).
4. E. E. Kwan, Y. Zeng, H. A. Besser, E. N. Jacobsen, Concerted nucleophilic aromatic substitutions. *Nat. Chem.* **10**, 917–923 (2018).
5. R. Sustmann, M. Dern, R. Kasten, W. Sicking, Charge-transfer complexes and reactivity in Diels-Alder cycloadditions. *Chem. Ber. Recl.* **120**, 1315–1322 (1987).
6. K. N. Houk, Frontier molecular orbital theory of cycloaddition reactions. *Acc. Chem. Res.* **8**, 361–369 (2002).
7. K. Black, P. Liu, L. Xu, C. Doubleday, K. N. Houk, Dynamics, transition states, and timing of bond formation in Diels-Alder reactions. *Proc. Natl. Acad. Sci. U.S.A.* **109**, 12860–12865 (2012).
8. Y.-F. Yang, P. Y. Yu, K. N. Houk, Computational exploration of concerted and zwitterionic mechanisms of Diels-Alder reactions between 1,2,3-triazines and enamines and acceleration by hydrogen-bonding solvents. *J. Am. Chem. Soc.* **139**, 18213–18221 (2017).
9. P. Y. Yu, C. Q. He, A. Simon, W. Li, R. Mose, M. K. Thøgersen, K. A. Jørgensen, K. N. Houk, Organocatalytic [6+4] cycloadditions via zwitterionic intermediates: Chemo-, regio-, and stereoselectivities. *J. Am. Chem. Soc.* **140**, 13726–13735 (2018).
10. R. Meir, H. Chen, W. Lai, S. Shaik, Oriented electric fields accelerate Diels-Alder reactions and control the *endo/exo* selectivity. *ChemPhysChem* **11**, 301–310 (2010).

11. N. Xin, J. Wang, C. Jia, Z. Liu, X. Zhang, C. Yu, M. Li, S. Wang, Y. Gong, H. Sun, G. Zhang, Z. Liu, G. Zhang, J. Liao, D. Zhang, X. Guo, Stereoelectronic effect-induced conductance switching in aromatic chain single-molecule junctions. *Nano Lett.* **17**, 856–861 (2017).

12. B. J. Sussman, D. Townsend, M. Y. Ivanov, A. Stolow, Dynamic stark control of photochemical processes. *Science* **314**, 278–281 (2006).

13. S. Schmaus, A. Bagrets, Y. Nahas, T. K. Yamada, A. Bork, M. Bowen, E. Beaurepaire, F. Evers, W. Wulfhekel, Giant magnetoresistance through a single molecule. *Nat. Nanotechnol.* **6**, 185–189 (2011).

14. C. Li, Z. Wang, Y. Lu, X. Liu, L. Wang, Conformation-based signal transfer and processing at the single-molecule level. *Nat. Nanotechnol.* **12**, 1071–1076 (2017).

15. S. Ciampi, N. Darwish, H. M. Aitken, I. Díez-Pérez, M. L. Coote, Harnessing electrostatic catalysis in single molecule, electrochemical and chemical systems: A rapidly growing experimental tool box. *Chem. Soc. Rev.* **47**, 5146–5164 (2018).

16. J. Joy, T. Stuyver, S. Shaik, Oriented external electric fields and ionic additives elicit catalysis and mechanistic crossover in oxidative addition reactions. *J. Am. Chem. Soc.* **142**, 3836–3850 (2020).

17. S. Shaik, D. Danovich, J. Joy, Z. Wang, T. Stuyver, Electric-field mediated chemistry: Uncovering and exploiting the potential of (oriented) electric fields to exert chemical catalysis and reaction control. *J. Am. Chem. Soc.* **142**, 12551–12562 (2020).

18. S. Shaik, R. Ramanan, D. Danovich, D. Mandal, Structure and reactivity/selectivity control by oriented-external electric fields. *Chem. Soc. Rev.* **47**, 5125–5145 (2018).

19. A. C. Aragonès, N. L. Haworth, N. Darwish, S. Ciampi, N. J. Bloomfield, G. G. Wallace, I. Diez-Perez, M. L. Coote, Electrostatic catalysis of a Diels-Alder reaction. *Nature* **531**, 88–91 (2016).

20. X. Y. Huang, C. Tang, J. Li, L.-C. Chen, J. Zheng, P. Zhang, J. Le, R. Li, X. Li, J. Liu, Y. Yang, J. Shi, Z. Chen, M. Bai, H.-L. Zhang, H. Xia, J. Cheng, Z.-Q. Tian, W. Hong, Electric field–induced selective catalysis of single-molecule reaction. *Sci. Adv.* **5**, eaaw3072 (2019).

21. C. Jia, B. Ma, N. Xin, X. Guo, Carbon electrode-molecule junctions: A reliable platform for molecular electronics. *Acc. Chem. Res.* **48**, 2565–2575 (2015).

22. Y. Li, C. Yang, X. Guo, Single-molecule electrical detection: A promising route toward the fundamental limits of chemistry and life science. *Acc. Chem. Res.* **53**, 159–169 (2020).

23. H. M. Wen, W. Li, J. Chen, G. He, L. Li, M. A. Olson, A. C.-H. Sue, J. F. Stoddart, X. Guo, Complex formation dynamics in a single-molecule electronic device. *Sci. Adv.* **2**, e1601113 (2016).

24. C. Zhou, X. Li, Z. Gong, C. Jia, Y. Lin, C. Gu, G. He, Y. Zhong, J. Yang, X. Guo, Direct observation of single-molecule hydrogen-bond dynamics with single-bond resolution. *Nat. Commun.* **9**, 807 (2018).

25. J. Guan, C. Jia, Y. Li, Z. Liu, J. Wang, Z. Yang, C. Gu, D. Su, K. N. Houk, D. Zhang, X. Guo, Direct single-molecule dynamic detection of chemical reactions. *Sci. Adv.* **4**, eaar2177 (2018).

26. C. Gu, C. Hu, Y. Wei, D. Lin, C. Jia, M. Li, D. Su, J. Guan, A. Xia, L. Xie, A. Nitzan, H. Guo, X. Guo, Label-free dynamic detection of single-molecule nucleophilic-substitution reactions. *Nano Lett.* **18**, 4156–4162 (2018).

27. L. Gaudreau, K. J. Tielrooij, G. E. D. K. Prawiroatmodjo, J. Osmond, F. J. G. de Abajo, F. H. L. Koppens, Universal distance-scaling of nonradiative energy transfer to graphene. *Nano Lett.* **13**, 2030–2035 (2013).

28. A. Brenneis, L. Gaudreau, M. Seifert, H. Karl, M. S. Brandt, H. Huebl, J. A. Garrido, F. H. L. Koppens, A. W. Holleitner, Ultrafast electronic readout of diamond nitrogen–vacancy centres coupled to graphene. *Nat. Nanotechnol.* **10**, 135–139 (2015).

29. M. J. Rust, M. Bates, X. Zhuang, Sub-diffraction-limit imaging by stochastic optical reconstruction microscopy (STORM). *Nat. Methods* **3**, 793–796 (2006).

30. A. Aviram, M. A. Ratner, Molecular rectifiers. *Chem. Phys. Lett.* **29**, 277–283 (1974).

31. K. D. Dubey, T. Stuyver, S. Kalita, S. Shaik, Solvent organization and rate regulation of a menshutkin reaction by oriented external electric fields are revealed by combined md and qm/mm calculations. *J. Am. Chem. Soc.* **142**, 9955–9965 (2020).

32. Y. Zang, Q. Zou, T. Fu, F. Ng, B. Fowler, J. Yang, H. Li, M. L. Steigerwald, C. Nuckolls, L. Venkataraman, Directing isomerization reactions of cumulenes with electric fields. *Nat. Commun.* **10**, 4482 (2019).

33. L. S. Milescu, A. Yildiz, P. R. Selvin, F. Sachs, Maximum likelihood estimation of molecular motor kinetics from staircase dwell-time sequences. *Biophys. J.* **91**, 1156–1168 (2006).

34. R. C. Boutelle, B. H. Northrop, Substituent effects on the reversibility of furan–maleimide cycloadditions. *J. Org. Chem.* **76**, 7994–8002 (2011).

35. Y. Xie, H. Zhao, Y. Wang, Y. Huang, T. Wang, X. Xu, C. Xiao, Z. Sun, D. H. Zhang, X. Yang, Quantum interference in H+HD → H₂+D between direct abstraction and roaming insertion pathways. *Science* **368**, 767–771 (2020).

36. F. Toshimitsu, H. Ozawa, N. Nakashima, Hybrids of copolymers of fluorene and C₆₀-carrying-carbazole with semiconducting single-walled carbon nanotubes. *Chemistry* **21**, 3359–3366 (2015).

37. L. Zou, J. A. Liu, K. Zhang, Y. Chen, F. Xi, Cyclopolymerization of α,ω-heterodifunctional monomers containing styrene and maleimide moieties. *J. Polym. Sci. A Polym. Chem.* **52**, 330–338 (2014).

38. Y. Zhao, D. G. Truhlar, The M06 suite of density functionals for main group thermochemistry, thermochemical kinetics, noncovalent interactions, excited states, and transition elements: Two new functionals and systematic testing of four M06-class functionals and 12 other functionals. *Theor. Chem. Acc.* **120**, 215–241 (2008).

39. A. V. Marenich, C. J. Cramer, D. G. Truhlar, Universal solvation model based on solute electron density and on a continuum model of the solvent defined by the bulk dielectric constant and atomic surface tensions. *J. Phys. Chem. B* **113**, 6378–6396 (2009).

40. Tian Lu, Molclus program, version 1.8.8, www.keinsci.com/research/molclus.html.

41. C. Jia, J. Wang, C. Yao, Y. Cao, Y. Zhong, Z. Liu, Z. Liu, X. Guo, Conductance switching and mechanisms in single-molecule junctions. *Angew. Chem. Int. Ed.* **52**, 8666–8670 (2013).

42. S. Smidstrup, T. Markussen, P. Vancraeyveld, J. Wellendorff, J. Schneider, T. Gunst, B. Verstichel, D. Stradi, P. A. Khomyakov, U. G. Vej-Hansen, M.-E. Lee, S. T. Chill, F. Rasmussen, G. Penazzi, F. Corsetti, A. Ojanperä, K. Jensen, M. L. N. Palsgaard, U. Martinez, A. Blom, M. Brandbyge, K. Stokbro, QuantumATK: An integrated platform of electronic and atomic-scale modelling tools. *J. Phys. Condens. Matter* **32**, 015901 (2020).